Talanta 119 (2014) 320–330

Contents lists available at ScienceDirect

Talanta

journal homepage: www.elsevier.com/locate/talanta

Combination of UV–vis spectroscopy and chemometrics to understand protein–nanomaterial conjugate: A case study on human serum albumin and gold nanoparticles

Yong Wang [a,b], Yongnian Ni [a,b,*]

[a] State Key Laboratory of Food Science and Technology, Nanchang University, Nanchang 330047, China
[b] Department of Chemistry, Nanchang University, Nanchang 330031, Jiangxi, China

ARTICLE INFO

Article history:
Received 16 September 2013
Received in revised form
4 November 2013
Accepted 7 November 2013
Available online 13 November 2013

Keywords:
Protein nanoconjugate
Chemometrics
UV–vis spectroscopy
Gold nanoparticles
Biosensor
Thermodynamics

ABSTRACT

Study of the interactions between proteins and nanomaterials is of great importance for understanding of protein nanoconjugate. In this work, we choose human serum albumin (HSA) and citrate-capped gold nanoparticles (AuNPs) as a model of protein and nanomaterial, and combine UV–vis spectroscopy with multivariate curve resolution by an alternating least squares (MCR-ALS) algorithm to present a new and efficient method for comparatively comprehensive study of evolution of protein nanoconjugate. UV–vis spectroscopy coupled with MCR-ALS allows qualitative and quantitative extraction of the distribution diagrams, spectra and kinetic profiles of absorbing pure species (AuNPs and AuNPs–HSA conjugate are herein identified) and undetectable species (HSA) from spectral data. The response profiles recovered are converted into the desired thermodynamic, kinetic and structural parameters describing the protein nanoconjugate evolution. Analysis of these parameters for the system gives evidence that HSA molecules are very likely to be attached to AuNPs surface predominantly as a flat monolayer to form a stable AuNPs–HSA conjugate with a core–shell structure, and the binding process takes place mainly through electrostatic and hydrogen-bond interactions between the positively amino acid residues of HSA and the negatively carboxyl group of citrate on AuNPs surface. The results obtained are verified by transmission electron microscopy, zeta potential, circular dichroism spectroscopy and Fourier transform infrared spectroscopy, showing the potential of UV–vis spectroscopy for study of evolution of protein nanoconjugate. In parallel, concentration evolutions of pure species resolved by MCR-ALS are used to construct a sensitive spectroscopic biosensor for HSA with a linear range from 1.8 nM to 28.1 nM and a detection limit of 0.8 nM.

1. Introduction

Exploration and development of the bio–nano interfaces between biocomponents and nanomaterials have important academic and practical significance in the field of chemistry, materials science and biology [1]. In the last few years, considerable scientific attention has been paid to the integration of proteins with nanomaterials to form protein nanoconjugates [2–4]. The protein nanoconjugate possesses numerous potential applications related to bioanalytical science [5–7], biosensors [8–10], biocatalysis [11–13], biofuel cells [14,15] and bio-based nanodevices [16,17]. The central focus, however implicit in most of these researches, is firmly on understanding how these proteins interact with nanomaterials [18,19].

An important aspect of this problem is to qualitatively and quantitatively know about thermodynamic, kinetic and structural information of proteins that binds to the nanomaterials [18,19]. To achieve the goal, various interactions of proteins and nanomaterials have been probed during the past years using a range of different analytical techniques [20,21], including nuclear magnetic resonance, quartz crystal microbalance, mass spectroscopy, circular dichroism spectroscopy, microscopy, surface plasmon resonance, separation-based, thermal-based, and scattering-based techniques.

However, almost all techniques cannot simultaneously give important information about thermodynamics, kinetics and structural aspects of the binding process of protein–nanomaterial conjugate. In addition, most of these techniques require sophisticated instrumentation, have relatively high analytical costs, involve cumbersome pretreatment procedures prior to the analysis or ex situ complicated operations, and some techniques show poor sensitivity in practical applications. Therefore, the development of a universal means to provide comparatively comprehensive descriptions of protein nanoconjugate formation is always

* Corresponding author at: Department of Chemistry, Nanchang University, 999 Xuefu Rd., Nanchang 330031, China. Tel./fax: +86 791 83969500.
E-mail address: ynni@ncu.edu.cn (Y. Ni).

0039-9140/$ - see front matter © 2013 Elsevier B.V. All rights reserved.
http://dx.doi.org/10.1016/j.talanta.2013.11.026

attractive, especially if the analytical technique is in situ, less complicated, cost-effective and relatively fast.

UV–vis spectroscopy is one of the most common techniques used for conventional analysis. To date, considerable literature has presented its application for research on protein nanoconjugates [20–25]. However, the technique usually provides only a limited amount of qualitative information on binding of protein to nanomaterials by observation of peak shift, broadening of the absorption spectra and spectral intensity variations [20–25]. And quantitative results on the binding are difficult to achieve likely because of very subtle changes in spectra, severe spectral overlap of optically coexisting species and spectral analysis in a univariate mode. Thus, there is an urgent need to find an effective tool to extract implicit information about thermodynamics, kinetics and structure of protein attachment onto nanomaterials from the collected spectral data quantitatively.

Chemometrics, generally known as multivariate statistics analysis, is an exploratory advanced tool to extract multiplex information of pure chemical species directly from the measured overlapping signals of complex systems without any previous physical or chemical separation [26–28]. Most chemometrics methods belong to the self-modeling or model-free methods, which are mainly factor analysis methods that easily meet the intrinsic property of the measurement and their multivariate data structure [26–28]. Among them, multivariate curve resolution by an alternating least squares (MCR-ALS) algorithm developed by Tauler and co-workers [29] is the most widespread used method, predominantly because the method is versatile, robust and rather flexible in dealing with many kinds of complex data structures and chemical problems, requires no priori knowledge or model about the studied system, and provides much qualitative and quantitative information with physical or chemical meaning to allow a full interpretation of the studied complex systems. The only requirements for MCR-ALS application are that data structure should conform to a given bilinear model, and some general knowledge about chemical features and the internal mathematical structure of the system studied, such as non-negativity, implying that all spectra take positive values, should be given [29]. Spectroscopy follows an additive nature of Beer–Lambert's law and has a typical bilinear data structure, so it fulfills well the requirements for application of MCR-ALS.

A detailed explanation of the MCR-ALS algorithm applied for spectral data resolution has been described in previous works [29–34]. Herein, we give only some relevant aspects of the algorithm for brevity.

The mathematical model established by the algorithm usually takes three steps. The first step is to determine the number of optically pure species that the evolving system possesses. This can be usually achieved by means of singular value decomposition [29] and the theory of error in factor analysis [35]. The second step is the construction of an initial estimate of concentration evolutions or spectra of the pure component present in a system. The estimate can be obtained from chemometrics techniques based on evolving factor analysis (EFA) or the purest variables or techniques based on the selection of representative spectra or evolving curves from chemical insight about the process. Finally, once the initial estimate is generated, an iterative alternating least squares (ALS) optimization step is carried out until convergence is achieved. During this iterative process, the introduction of constraints is of crucial importance to obtain physically or chemically meaningful evolving profiles and spectra and to drive the optimization to the sought solution, decreasing the rotational and intensity ambiguities of the resolved profiles. The main constraints are non-negativity, unimodality (the presence of only a single maximum per profile or a plateau-like maximum), closure (the mass balance for total concentration along the evolving process), selectivity or local rank information (some species are forced to be absent in some ranges of resolving profiles based on known information, such as at the beginning and end of the evolving process), component correspondence (the information related to the species in the different samples; if known, set the absent species to be null) and trilinearity (the resolved profiles of the same component in the different data matrices for a particular dimension) [29].

Another outstanding feature of the MCR-ALS method is that it can be easily extended to the simultaneous analysis of multiexperiments under different conditions and/or together with simpler subsystems, by column-wise data matrix augmentation [29]. Generally, column-wise augmented data matrices can be accomplished by appending matrices, belonging to different processes, one on top of each other. They share common spectra in a particular technique (e.g. UV–vis spectroscopic technique), but lengthen in the process directions. The augmented matrices were demonstrated to be able to minimize the ambiguities and remove the rank deficiency problem associated with the decomposition of a single data matrix, and allow reliable and accurate estimation of the number of pure components and description of the chemical evolving system.

During the past few years, spectroscopy coupled with a MCR-ALS tool has been a common phenomenon, and has been satisfactorily applied to study biocomponents or nanomaterials of complex systems involving equlibria or kinetic chemical process [30–34]. To the best of our knowledge, there are, however, no literature reports on investigating the thermodynamics, kinetics and structure of protein nanoconjugate evolution in detail by spectroscopy combined with MCR-ALS. In this context, we herein make an attempt to establish a universal method for integrated research into the evolutionary processes of the protein nanoconjugate using UV–vis spectroscopy together with the MCR-ALS technique. The powerful resolution advantage of MCR-ALS allows extracting distribution diagrams, spectra and kinetic profiles of pure species of interest involved in the evolutionary process. The distribution diagrams can provide quantitative thermodynamic information about equilibrium constant, stoichiometry, molecule footprint, standard free energy change (ΔG), standard enthalpy change (ΔH) and standard entropy (ΔS) change of the binding of protein to nanomaterials, and about possible arrangement and orientation information (monolayer or multilayer structure and “flat-on” or “end-on” conformation) of protein attached to the surface of nanomaterials. The kinetic profiles can present quantitative information about the formation mechanism of protein nanoconjugate, such as reaction rate constant, reaction order, reaction activation energy and so on. The features of the recovered pure spectra (molar extinction coefficient, peak wavelength, peak width and peak shape) can help in the qualitative analysis of structural characteristics of the species of interest involved.

As a case study, human serum albumin (HSA) and citrate-capped gold nanoparticles (AuNPs) are respectively selected as a model of protein and nanomaterial. HSA is readily available and the most abundant protein in the circulatory system, and its related structural information (for example, HSA is a prism-shaped-structure protein of dimensions 8.4 nm × 8.4 nm × 3.15 nm) [36,37] has been better understood. Citrate-capped AuNPs have well-established synthesis methods, and possess good optical and electronic properties [38]. Concurrent with our study of protein–nanomaterial interaction, citrate-capped AuNPs are exploited as spectrophotometric probes to fabricate a biosensor for sensitive detection of HSA.

2. Materials and methods

2.1. Reagents and chemicals

Chloroauric acid tetrahydrate and trisodium citrate dihydrate were purchased from Sinopharm Chemical Reagent Co. (Shanghai,

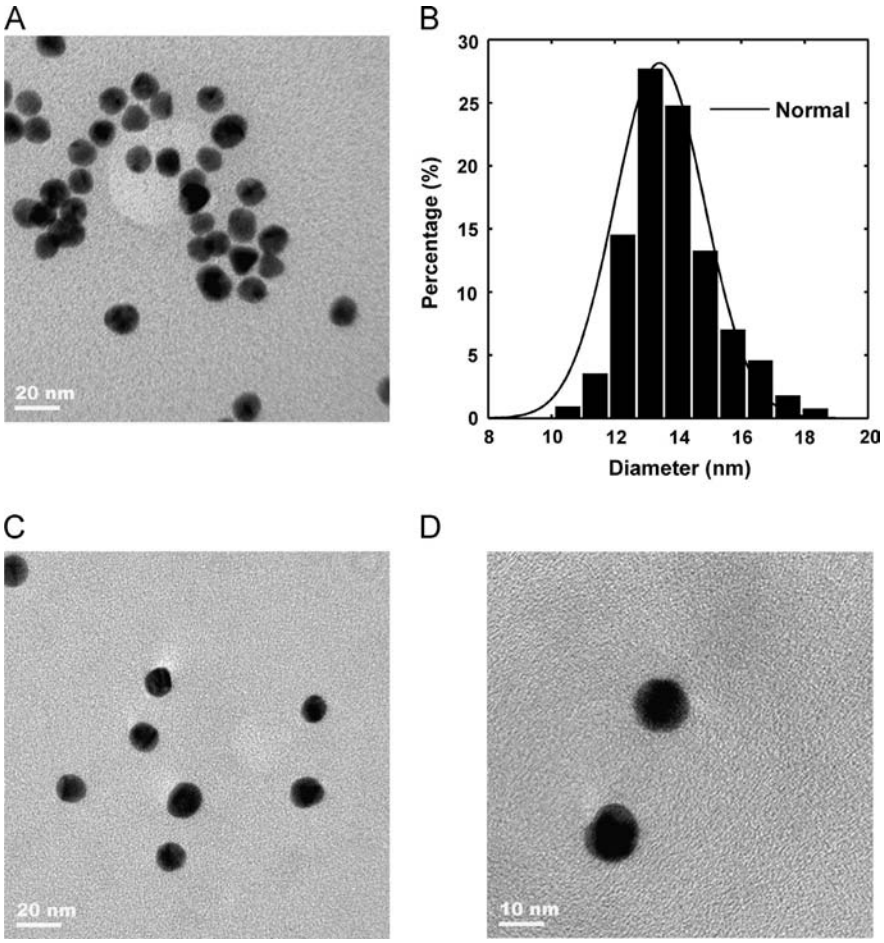

Fig. 1. (A) TEM image of citrate-capped AuNPs. (B) Corresponding histogram of particle size distribution for AuNPs and its fitted normal distribution curve. (C) TEM image of citrate-capped AuNPs in the presence of HSA. (D) Enlarged TEM image derived from (C). A soft gray-colored outer region around the high electron-density dark black-colored inner region can be observed.

China). Human serum albumin (HSA) was obtained from Solarbio Science & Technology Co. (Beijing, China). Unless specified otherwise, all other chemicals were of analytical reagent grade and used as received. Double distilled water was used throughout the course of investigation. An HSA solution (1.0 mM) was prepared by dissolving 0.3323 g of the purified protein (MW=66,450 Da) in 5.0 mL water and stored at 4 °C in dark. It was diluted to desired concentrations for practical use. Accurate concentration of the HSA solution was determined by measuring the UV absorbance at 278 nm ($\varepsilon_{HSA}=3.44\times10^4\ M^{-1}\ cm^{-1}$) [39].

2.2. Synthesis of AuNPs

All glasswares employed in the preparation were cleaned in a bath of freshly prepared aqua regia ($HCl/HNO_3=3:1$, v/v), rinsed thoroughly in water, and oven-dried prior to use. AuNPs were prepared by citrate reduction of chloroauric acid [40]. An aqueous solution of chloroauric acid tetrahydrate (10.3 mL, 1%) was added to 255 mL water and mixed thoroughly. Subsequently, the solution was brought to a rolling boil with stirring. The rapid addition of a trisodium citrate solution (9.5 mL, 3%) to the vortex of the solution resulted in a color change from pale yellow to deep red. The boiling was continued for 15 min; then the solution was removed from the heating mantle, and stirring was continued for an additional 30 min. The solution was then allowed to cool naturally to room temperature. The resulting deep red solution was stored in a refrigerator at 4 °C before use. Of note, the solution pH level of citrate-capped AuNPs was maintained at about 6.5 [41].

The morphology and size of as-prepared AuNPs were measured by transmission electron microscopy (TEM) imaging. A representative TEM image of the AuNPs (Fig. 1A) displayed well-distributed spherical and nearly monodispersed nanocrystals with a diameter of 13.4 ± 1.4 nm (note that in this study the standard deviation of AuNP size was calculated based on more than 500 nanoparticles in the TEM images). Correspondingly, the particle size distribution histogram of the AuNPs is shown in Fig. 1B. For comparison, the curve indicating the expected normal distribution was also added. And these TEM results are in substantial agreement with their surface plasmon resonance (SPR) spectrum, which has characteristic peak wavelength at 519 nm. The concentration of AuNPs was calculated to be 15.6 nM by UV–vis spectroscopy based on the extinction coefficient of $2.4\times10^8\ M^{-1}\ cm^{-1}$ at 519 nm [42].

2.3. Instrumentation

Kinetic and UV–vis spectral measurements were performed on an Agilent 8453 UV–vis spectrometer equipped with a Model ZC-10 (Ningbo Tianheng Instruments, China) temperature control accessory and a 10 mm quartz cuvette. Transmission electron microscopy (TEM) was performed by a JEM-2010 microscope operated at an accelerating voltage of 200 kV. The samples for TEM were prepared by pipetting 10 μL of colloidal solution onto a carbon-coated copper grid, and dried overnight at room temperature. The measurements of zeta potential were performed using a PSA NANO2590 apparatus (Malvern Instruments Ltd., England). Circular dichroism spectra (CD) were recorded on a Bio-Logic MOS

450 spectropolarimeter (Bio-Logic, France) using a 1.0 mm quartz cuvette. Fourier transform infrared spectroscopy (FT-IR) was collected in the transmission mode with KBr as scanning matrix on a Nicolet 380 FT-IR spectrometer (Thermo Nicolet Corporation, USA) equipped with a DTGS KBr detector. The samples for FT-IR were prepared by placing 5 μL of HSA or colloidal solution on KBr pellets and dried to remove water.

2.4. UV–vis spectral measurements of AuNPs–HSA conjugate evolution

In a typical analysis of AuNPs–HSA conjugate evolution, 1.5 mL of water and 370 μL of AuNPs solution (pH 6.5) were micropipetted into a 3.5 mL cuvette, and incubated for 2 min. Subsequently, HSA solution was added to give a series of samples with different concentrations (c_{HSA}=0–70.3 nM; total 13 samples). The absorbance data of the solution were measured immediately after the addition of HSA. All spectral-kinetic data were collected simultaneously from 240 nm to 900 nm every 1 nm, at 5 s intervals for 480 s using water as a blank. The mixture solution was stirred throughout the experiment. All assays were performed at three temperatures (298.15 K, 303.15 K and 308.15 K).

2.5. Chemometrics analysis for the protein nanoconjugate system

For systematic and comparative study of the evolving process of protein nanoconjugate, the entire time-dependent evolutions of UV–vis spectra for n samples at constant temperature are monitored at different molar ratios of nanomaterial to protein, where the concentration of nanomaterial is kept unchanged, but the concentration of protein is varied. Correspondingly, the kinetic spectral data matrices related to the n mole-ratio experiments, $\mathbf{D}_1$, $\mathbf{D}_2$, …, $\mathbf{D}_n$, can be built up (Scheme 1). These data sets containing mixture information are arranged as a column-wise augmented matrix of size $(n \times k) \times m$, $\mathbf{D}_{aug}$, with k rows as the number of recorded UV–vis spectra and m columns as kinetic profiles scanned during the spectral measurements. The knowledge of reaction thermodynamics points out that the concentrations of chemical species are kept unchanged at the conclusion of a chemical reaction. Usually, this means that reaction equilibrium is achieved at a plateau-like maximum of reaction kinetics, i.e., at temporal end-point of the measurement. To fully understand thermodynamic aspects of the evolving system, the absorbance data for temporal end-point in the mole-ratio experiments are herein selected to construct a new data matrix of size $n \times m$, $\mathbf{D}$ (Scheme 1A). As can be seen, the concentration evolutions and spectra of various absorbing pure species represented in the form of $\mathbf{C}$ matrix (size $n \times nc$, nc denotes number of spectroscopically active components existing in this system) and $\mathbf{S}^T$ matrix (size $nc \times m$) can be extracted from the constructed data matrix using the MCR-ALS algorithm. Moreover, to study the kinetic aspect of the system in detail, the raw augmented matrix, $\mathbf{D}_{aug}$, is required to be analyzed carefully (Scheme 1B). Because all experiments analyzed together were carried out under the same condition, the same absorbing components have identical spectra in each experiment. Mathematically, this means that in this matrix augmentation, common vectors span the column vector spaces of the different individual data matrices, i.e., the spectral matrix, $\mathbf{S}^T$ (size $nc \times m$), is the same for each data set. Under this premise, the augmented evolution matrix of size $(n \times k) \times m$, $\mathbf{C}_{aug}$, can be derived from the raw augmented matrix, $\mathbf{D}_{aug}$, by use of the MCR-ALS method. Simultaneously, this resolution results in an augmented error matrix of size $(n \times k) \times m$, $\mathbf{E}_{aug}$. Subsequently, the augmented evolution matrix can be rearranged to n small matrix of size $k \times nc$, $\mathbf{C}_1$, $\mathbf{C}_2$, …, $\mathbf{C}_n$, containing kinetic profiles for various spectroscopically active species in the system. Finally, all these resolved profiles can be further used to deduce various kinetic, thermodynamic and structural parameters, which is helpful for comprehensive analyses and interpretations of the protein nanoconjugate studied.

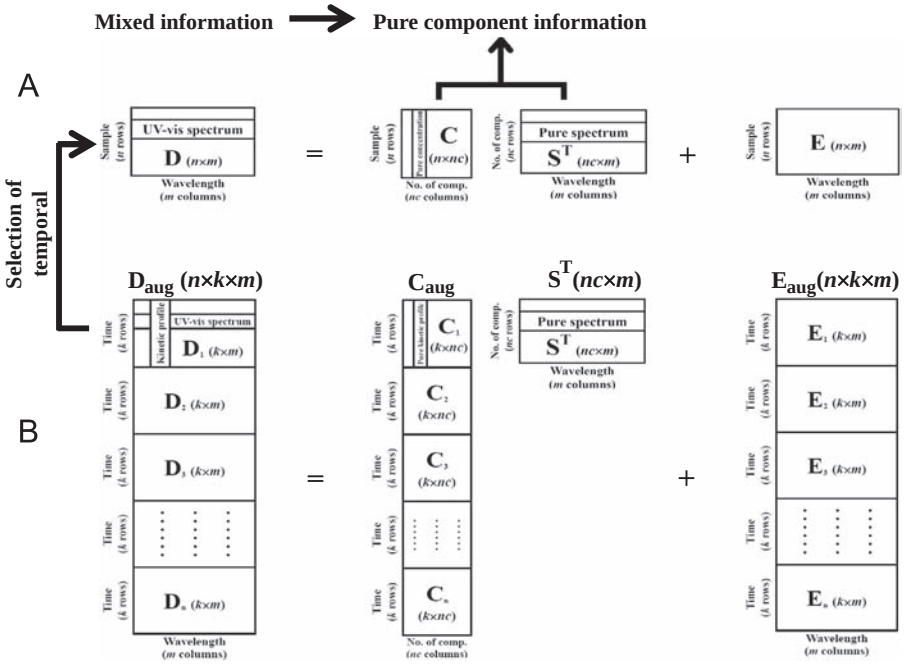

Scheme 1. Procedure for MCR-ALS analysis of the time-dependent UV–vis spectral data of nanomaterial–protein corona. (A) Application of MCR-ALS to a single data matrix, **D**, that is constructed by spectral data at temporal end-point in n mole-ratio experiments. **C** and **S** denote the concentration and spectral matrices of various absorbing pure species in the chemical evolving process, respectively. **E** is an error matrix. (B) Application of MCR-ALS to a column-wise augmented data matrix, $\mathbf{D}_{aug}$, which is constructed by n temporal-spectral data matrix ($\mathbf{D}_1$, $\mathbf{D}_2$, $\mathbf{D}_3$… $\mathbf{D}_n$) related to mole-ratio experiments. $\mathbf{C}_{aug}$ represents the augmented evolution matrix of absorbing pure species that can be rearranged to n small kinetic matrices ($\mathbf{C}_1$, $\mathbf{C}_2$, $\mathbf{C}_3$ … $\mathbf{C}_n$). **S** and $\mathbf{E}_{aug}$ are the spectral matrix of absorbing pure species and the augmented error matrix, respectively.

In the work, the ALS optimization is stopped when the relative difference in the standard deviations of the residuals between the experimental and the MCR-ALS reproduced data in two consecutive iterations is below a threshold value. The quality of the MCR-ALS model is evaluated by two indicators, i.e., the percentage of lack of fit (LOF) and the percentage of explained variance (R^2), which are defined below [29]:

$$\text{LOF}\ (\%) = 100\sqrt{\sum_{i,j} e_{ij}^2 / \sum_{i,j} d_{ij}^2} \quad (1)$$

$$R^2\ (\%) = 100\left(1 - \sqrt{\sum_{i,j} e_{ij}^2 / \sum_{i,j} d_{ij}^2}\right) \quad (2)$$

where d_{ij} and e_{ij} refer to an element of the input data matrix **D** and the associated residual given by difference between the input element and the reproduction from $\mathbf{CS}^{\mathrm{T}}$ product estimated using the MCR-ALS method, respectively. Subscripts i and j indicate the rows and columns of the original data matrix, respectively.

The similarity coefficient (r), which represents the correlation between the resolved profiles and the known references, is also applied to assess the quality of the resolved profiles:

$$r = \cos\,\gamma = \frac{\boldsymbol{x}_i^{\mathrm{T}} . \hat{\boldsymbol{x}}_i}{||\boldsymbol{x}_i^{\mathrm{T}}||||\hat{\boldsymbol{x}}_i||} \quad (3)$$

where γ is the angle of the vectors related to the profile recovered by MCR-ALS ($\hat{\boldsymbol{x}}_i$) and the true profile ($\boldsymbol{x}_i$), for a certain species.

In general, when the values of LOF, R^2 and r are close to 0, 1, and 1, respectively, the best modeling fitting of the experimental data is achieved, suggesting that good resolution results without ambiguities are obtained. Noticeably, a similarity value of 1 means that the angle between two vectors is 0, and thus, there is a perfect agreement between the recovered profile and the known true profile.

3. Results and discussion

3.1. Physicochemical characterization and preliminary analysis of AuNPs–HSA conjugate

UV–vis absorption spectroscopy is the most widely used method for characterizing the optical properties of nanomaterials and investigating protein nanoconjugate, because the intensity and position of the surface plasmon resonance (SPR) band of nanomaterials are related to the size, shape and aggregation of the nanomaterials, and highly sensitive to alterations in the surroundings of the nanomaterials [26,27]. In this work, a series of the temporal evolutions (0–480 s) of UV–vis spectra of AuNPs at 298.15 K were measured by holding the concentration of AuNPs constant and successively increasing HSA concentrations (Fig. 2A–M). It is clearly noted in Fig. 2A that the citrate-capped AuNPs exhibit a broad SPR band with a characteristic peak wavelength of 519 nm, which is substantially consistent with an earlier report [16]. Immediately following the HSA addition to the citrate-capped AuNPs, the peak intensity of the AuNPs increased subtly, accompanied by a very little bathochromic shift of the SPR peak (~2–4 nm) and a very small broadening of the SPR band in long wavelength region (Fig. 2B–M). After ~180 s of the reaction, the system reached a state of almost equilibrium in which there was essentially no appreciable spectral variations in the SPR feature (Fig. 2B–N). All these phenomena indicate that HSA binds to the surface of AuNPs to form a AuNPs–HSA conjugate. It is worth noting that a significant decrease of absorbance at peak wavelength or/and a considerable increase of absorbance at long wavelengths (600–700 nm) is/are not detected (see Fig. 2A–M), implying that there are no strong NP-to-NP interactions, and thus the AuNPs in the complex remain randomly dispersed rather than aggregated under current experimental conditions [26,27]. In addition, the UV–vis spectra at temporal end-point (480 s; Fig. 2O), which is extracted from the original kinetic spectra, clearly show that with the increase of HSA concentration, the SPR band of AuNPs progressively intensifies, broadens and red-shifts until reaching a stable/irreversible value, strongly suggesting that the formation of AuNPs–HSA conjugate is related to HSA concentration.

To further support the interpretations given by UV–vis absorption spectral data, two well-established noninvasive techniques, transmission electron microscopy (TEM) and zeta potential, were applied to systematically characterize the size of AuNPs and understand AuNPs–HSA conjugate. The TEM micrograph of AuNPs in the presence of HSA clearly shows that AuNPs remain as spherical nanocrystals and are well separated, denoting the absence of aggregation (Fig. 1C). The enlarged TEM image displays that there is a soft gray-colored outer region around the high electron-density dark black-colored inner region (Fig. 1D). This sharp contrast obtained by TEM measurements indicates that AuNPs are encapsulated by HSA to form a stable AuNPs–HSA corona with a core–shell structure. Data from zeta potential measurements show that the introduction of HSA to the AuNPs solution leads to a variation of zeta potential from −25.7 mV to −14.7 mV, close to that of the bare HSA solution (−16.0 mV). The results confirm that HSA molecules are very likely to bind on the AuNPs surface by an electrostatic mechanism through the positively charged amino acid residues of HSA (lysine, arginine and histidine) and the surface citrate anions [43]. Simultaneously, the absence of AuNP aggregates observed from TEM images (Fig. 1C) further shows that the stability of the AuNPs–HSA conjugate may be also mediated by steric repulsions between the associated HSA molecules, which prevents AuNPs from coming into contact. In general, all these results given by the two techniques are in line with those found by UV–vis spectral investigations, confirming the effectiveness of UV–vis absorption spectroscopy for analysis of protein–nanomaterial conjugate.

Circular dichroism spectroscopy (CD) and Fourier transform infrared spectroscopy (FT-IR) are two common methods to acquire information about protein conformations in solution and chemistry at the nano–bio interface. CD spectroscopic measurements of HSA were carried out in the absence or the presence of AuNPs. As shown in Fig. 3A, there is no CD spectrum in the case of AuNPs. This may be attributed to lack of any chiral center in the AuNPs structure, and therefore has no CD activity. Moreover, two negative bands in the ultraviolet region at 208 nm and 220 nm can be exhibited in the case of pure HSA, which are characteristics of α-helix structure of protein [44]. After the addition of AuNPs to HSA, there is a pronounced reduction in ellipticity of the band around 208 nm, indicating the loss of α-helix structure and the occurrence of HSA unfolding after the attachment to AuNPs.

FT-IR is profitably employed for detecting the conformational changes in the secondary structure of proteins by analysis of the specific stretching and bending vibrations of the peptide backbone in amide I (1600–1700 cm^{-1}) and II (1500–1600 cm^{-1}) bands. Data from transmission FT-IR spectra show that HSA possesses an IR spectrum with an amide I band around 1660 cm^{-1} and an amide II band around 1549 cm^{-1} (Fig. 3B), which originate from the C=O stretching, and coupling between C–N stretching and N–H bending modes, respectively [45]. And the citrate-capped AuNPs display a band around 1647 cm^{-1} (Fig. 3B), which is assigned to carboxylate asymmetric stretching vibration of citrate on the surface [46]. Addition of AuNPs to HSA gives rise to remarkable changes in peak position and band shape of HSA, resulting in asymmetrical broadening of amide I band to lower wavenumbers (from 1660 cm^{-1} to 1657 cm^{-1}) and a shift of amide II peak to higher wavenumbers (from 1549 cm^{-1} to 1552 cm^{-1}; Fig. 3B). In the absence of AuNPs, the amide I band

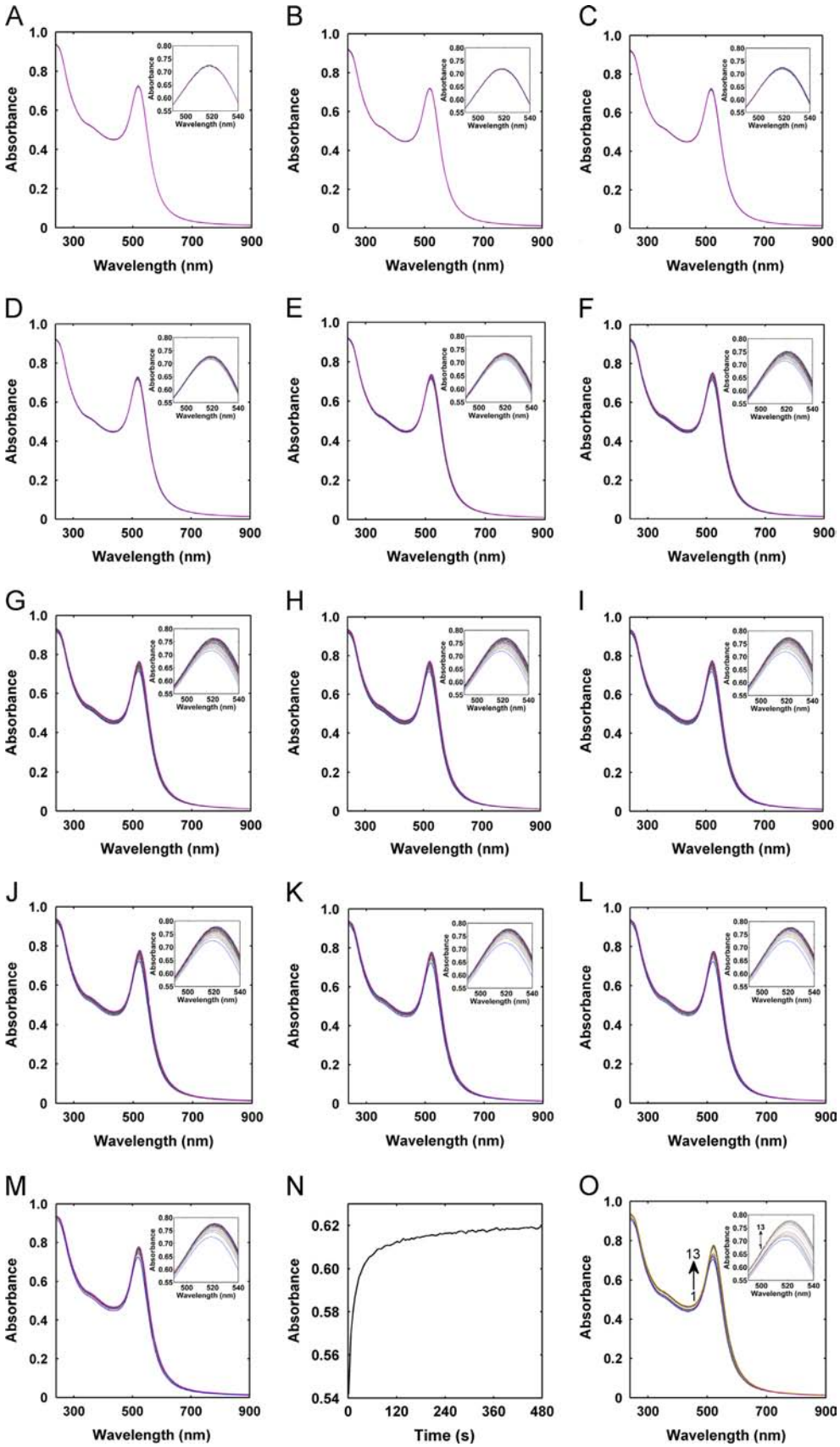

Fig. 2. Time-dependent UV–vis spectra of 2.95 nM AuNPs at 298.15 K with different concentrations (nM) of HSA: (A) 0, (B) 1.76, (C) 3.51, (D) 7.03, (E) 14.1, (F) 21.1, (G) 28.1, (H) 35.1, (I) 42.2, (J) 49.2, (K) 56.2, (L) 63.2, and (M) 70.3. (N) Kinetic profile at 545 nm under the experimental conditions in (M). (O) UV–vis spectra at temporal end-point derived from (A–M). Arrow indicates spectra with increasing HSA concentration. Inset: enlarged part of spectra in the 490–540 nm wavelength range.

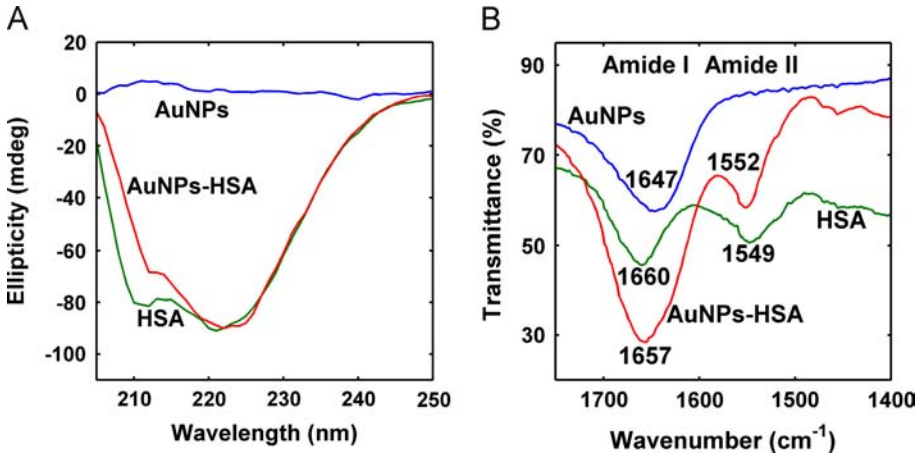

Fig. 3. (A) CD spectra of HSA (8 μM) and citrate-capped AuNPs (14.8 nM) with and without HSA. (B) FT-IR spectra of HSA (375 μM) and citrate-capped AuNPs (2.95 nM) with and without HSA.

centered at 1660 cm^{-1} denotes the significant α-helix content of HSA [45]. In the presence of AuNPs, the center of amide I band shifts down to 1657 cm^{-1}, possibly implying less compact structures of HSA on the AuNPs surface and the presence of citrate [45,46]. Noticeably, the shift of a center of amide II band to higher wavenumbers indicates that many hydrogen bonds are produced to affect predominantly N–H bending vibrations [47]. These data support the idea that during the evolution of HSA–AuNPs conjugate, the internal HSA hydrogen bonds break and the intermolecular hydrogen bonds between HSA and AuNPs are formed possibly by hydrogen bonding between the amino acid residues ($-NH_2$) of HSA and the carboxyl group (–COOH) of citrate on the surface of AuNPs, accompanied by simple loss of water of hydration [43,47].

3.2. *Thermodynamic study of AuNPs–HSA conjugate by UV–vis spectra at temporal end-point and MCR-ALS*

To propose the mechanism of the evolution of AuNPs–HSA conjugate, we herein employ a UV–vis spectroscopy technique for quantitative thermodynamics studies of HSA binding to AuNPs in detail. As mentioned above, the key to solving the problem lies in applying the MCR-ALS tool to recover spectra and concentration evolutions of absorbing pure species from the raw spectral data of a complex evolving system. Derived from the UV–vis spectral data at temporal end-point (Fig. 2O), the number of spectroscopically active pure species during the evolving process of protein nanoconjugate at 298.15 K can be first evaluated by error theory in factor analysis [35]. The noise level can be estimated to be around 0.0012 through the greatest contributions obtained in the selected wavelength range of 750–900 nm, where no SPR band is observed. The full-spectrum data are then analyzed by principal factor analysis, and the results show that Malinowski's real error (RE) related to the second abstract factor is calculated to be 0.00077, less than the expected noise value. This denotes two major absorbing species involved in the complex system, i.e., AuNPs and AuNPs–HSA conjugate. HSA is not likely to be responsible for the spectra of the complex system because compared with AuNPs, it almost does not give any measurable absorbance (the absorbance value is calculated to be below 0.0025 based on the molar extinction coefficient at 278 nm) in the given concentration range (0–70.3 nM), which is well consistent with the experiment result (see Fig. S1 in Supplementary material).

Given only two major absorbing species in the complex system, the spectra obtained at the beginning and end of the evolution process are selected as initial estimates of the later ALS iterative optimizations. Concomitantly, some constraints, such as non-negativity for both concentration evolutions and spectra, local rank information for concentration evolutions and normalization for spectra, are introduced in the optimization process to reduce rotational ambiguity. The optimum relative normalized concentration evolutions of pure species estimated with MCR-ALS method are presented in Fig. 4A. The quality parameters for the resolution give a lack of fit of 0.16% and a variance explained of 99.99%, suggesting that perfect resolution results are gained. The distribution diagram clearly shows that the relative concentration of AuNPs decreases significantly, that of HSA–AuNPs conjugate increases sharply and their concentrations reach saturation at ~11:1 molar binding stoichiometry between HSA and AuNPs.

Based on 11 protein binding sites per AuNP, we suppose that AuNPs–HSA conjugate is likely to follow the reaction mechanism

$$\mathrm{AuNPs} + 11\ \mathrm{HSA} \leftrightarrow \mathrm{AuNPs-HSA_{11}} \tag{4}$$

The binding equilibrium constant of the AuNPs–HSA complex can be calculated as follows:

$$K_b = \frac{[\mathrm{AuNPs-HSA_{11}}]}{[\mathrm{AuNPs}][\mathrm{HSA}]^{11}} \tag{5}$$

where [AuNPs], [AuNPs–HSA_{11}] and [HSA] correspond to the molar concentrations of AuNPs, AuNPs–HSA conjugate and HSA, respectively.

Assume that HSA has an equivalent and independent binding site on AuNPs, the apparent binding constant, K_{app}, of the nanobioconjugate, which is more understandable than the binding constant, K_b, for judging the binding ability, can be defined as follows:

$$K_{app} = \sqrt[11]{K_b} = \sqrt[11]{\frac{[\mathrm{AuNPs-HSA_{11}}]}{[\mathrm{AuNPs}][\mathrm{HSA}]^{11}}} \tag{6}$$

It is easy to find from Eqs. (5) and (6) that the absolute molar concentrations of various species are strongly required to calculate the binding constants. Fortunately, earlier work lets us know that the information about stoichiometric numbers of all species in the reaction and the known absolute concentration of AuNPs as reference allow us to deduce the absolute concentration evolutions and the spectra in absolute unit of all species, resulting in the elimination of intensity ambiguity [48].

Under this premise, the concentration evolutions in terms of absolute molar concentration and the spectra in terms of molar extinction coefficient of AuNPs and AuNPs–HSA conjugate are estimated and displayed in Fig. 4B and C. Noticeably, the absolute concentration evolution of the undetectable species in the complex

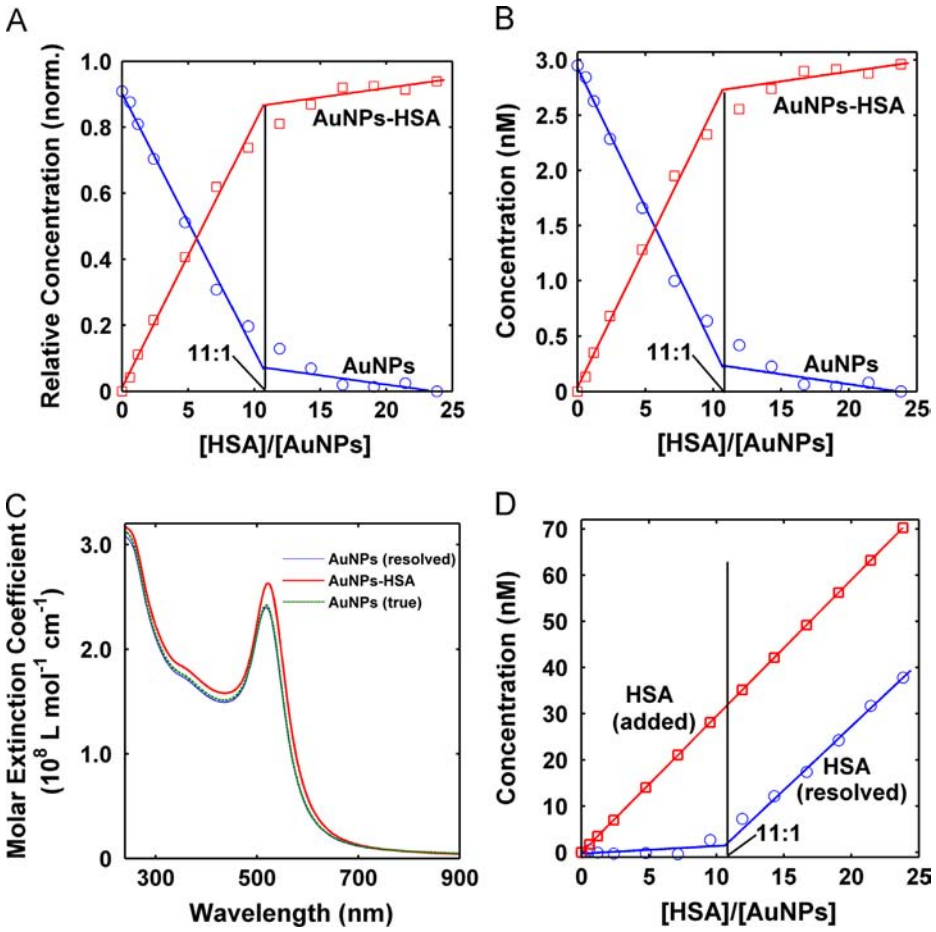

Fig. 4. (A) Relative concentration profiles of AuNPs and AuNPs–HSA conjugate recovered by MCR-ALS from a spectral single data matrix of 13 mole-ratio experiments at 298.15 K. (B) Resolved distribution diagram of AuNPs and AuNPs–HSA in terms of molar concentration. (C) Resolved spectra of AuNPs and AuNPs–HSA, and true spectra of AuNPs in terms of molar extinction coefficient. (D) Resolved distribution diagram and initial concentration profiles of HSA in terms of molar concentration.

system, HSA, can also be conveniently estimated by this method and the resolved distribution diagram is shown in Fig. 4D. Based on the calculation of the absolute concentration of all species in an equilibrium state, the apparent binding constant at 298.15 K can be estimated to be $8.4 \times 10^8\ M^{-1}$, which correlates well with earlier reports [49]. As can be clearly seen in Fig. 4C, there is almost no difference between the true spectra and resolved spectra in the case of AuNPs with the similarity coefficient of 0.9999, further giving evidence for the absence of rotational ambiguity in the resolution process. In addition, the SPR band of the AuNPs–HSA conjugate, relative to that of AuNPs, broadens, intensifies and red-shifts from 519 nm to 523 nm and this conjugate has a molar extinction coefficient of $2.6 \times 10^8\ M^{-1}\ cm^{-1}$ at peak wavelength, ~1.1-fold larger than that of AuNPs (Fig. 4C). Fig. 4D displays that the absolute concentrations of HSA are very low before the binding process reaches a steady state, and then they increase almost linearly with the increasing concentrations of HSA.

Further information about the structure of protein on the AuNPs surface can be extracted from the above resolution results. The actually average projected area occupied on the AuNPs surface by an individual HSA molecule, referred to as the molecular footprint, can be calculated from the division of the total surface area per AuNP by the saturated number of HSA molecules per AuNP. Derived from the diameter (13.4 nm) of the bare AuNPs measured from TEM, the radius of AuNPs is calculated to be 6.7 nm. And the total surface area per AuNP can be estimated to be about 564 nm^2 ($4\pi \times 6.7^2\ nm^2$). As discussed above, the saturated number of HSA molecules per AuNP is 11. Therefore, the actually saturated surface area per HSA molecules on AuNP can be calculated to be 51.3 nm^2. Following the equilateral triangular prism model with sides of 8.4 nm and a height of 3.15 nm for serum albumin in solution, the theoretical surface area per HSA molecule attached to the AuNP surface in a "flat-on" and "end-on" conformation approximates to 30.6 nm^2 ($1/2 \times 8.4^2 \sin(\pi/3)\ nm^2$) and 26.5 nm^2 ($3.15 \times 8.4\ nm^2$), respectively. Both theoretical surface area values are less than the actually saturated surface area value, suggesting that HSA is most likely inclined to lie flat on the AuNPs with a full monolayer coverage. In addition, according to the method previously proposed by Nienhaus's group [50], the theoretically saturated number, N, of the bound protein molecules for a monolayer coverage on a spherical nanoparticle can be estimated as follows:

$$N = \left[\left(\frac{R_N}{R_0}\right)^3 - 1\right]\frac{V_0}{V_p} \tag{7}$$

where R_N, R_0, V_p and V_0 represent, respectively, the radii of nanoparticle with and without protein, the volume of the bound protein molecule and the volume of nanoparticle without protein.

In this work, because the diameter of the bare AuNPs measured from TEM is 13.4 nm, the radius and the volume per AuNP are approximately equal to 6.7 nm and 1260 nm^3 ($4/3\pi \times 6.7^3\ nm^3$), respectively. Following the equilateral triangular prism model with sides of 8.4 nm and a height of 3.15 nm for serum albumin in solution [36,37], the volume per HSA molecule can be estimated to be close to 96.3 nm^3 ($3.15 \times 1/2 \times 8.4^2 \sin(\pi/3)\ nm^3$). The radius

per AuNPs–protein corona with HSA molecules attached to each AuNP in a "flat-on" and "end-on" conformation is approximately equal to 9.9 nm (6.7+3.15 nm) and 14.0 nm (6.7+8.4 × sin(π/3) nm), respectively. Thus, for surface full monolayer coverage, the theoretically saturated number of HSA molecules attached per AuNP in a "flat-on" and "end-on" conformation can be estimated to be about 29 and 106, respectively. Both values are greater than the actually saturated number obtained above, which is in good agreement with previous report [51]. The result implies that the AuNP surface is either void or linked to loosely bonded amino acid residues of HSA. The underestimate of the actually saturated number is presumably due to steric hindrance and electrostatic repulsion of neighboring HSA molecules attached to the AuNP surface.

In addition, a similar procedure is applied for the analysis of absorbance data of temporal end-point UV–vis spectral measurements at 303.15 K and 308.15 K (see Figs. S2 and S3 in Supplementary material). There remain only two major absorbing species, HSA and AuNPs–HSA conjugate, using error theory in factor analysis. The distribution diagrams and the spectra of all species at 303.15 K and 308.15 K resolved by MCR-ALS are shown in Figs. S4 and S5 (see Supplementary material). The values of lack of fit, variance explained and similarity coefficient at the two temperatures are below 0.16%, above 99.99% and above 0.9999, respectively, giving excellent resolution results. Looking at the resolved distribution diagrams and spectra in all experiments (297.15 K, 303.15 K and 308.15 K), it can be observed that they seem to be very similar. Quantitative comparison of the thermodynamic information derived from the resolutions at three temperatures, such as the binding ratio between HSA and AuNPs, and the apparent binding constants, are described in Table 1. It can be noted that the binding ratio is not basically affected by temperature, indicating that the thermodynamic mechanism may be not changed in the temperature range studied. However, the apparent binding constants decrease monotonically with temperature, showing that the intrinsic bond formation of AuNPs–HSA conjugate is exothermic. To further clearly delineate the potential molecular forces contributing to the formation of AuNPs–HSA conjugate, three thermodynamic quantities related to the formation of AuNPs–HSA conjugate, standard enthalpy change (ΔH), standard entropy change (ΔS) and standard Gibbs free energy change (ΔG), are clearly required.

Assuming that no significant changes in the enthalpy and the entropy over the temperature range are valid, the three thermodynamic parameters can be estimated from the following equations [52,53]:

$$\ln K_{app} = -\frac{\Delta H}{RT} + \frac{\Delta S}{R} \tag{8}$$

$$\Delta G = -RT \ln K_{app} \tag{9}$$

where R and T are the universal gas constant and the thermodynamic temperature, respectively; K_{app} denotes the apparent binding constants between AuNPs and HSA at the corresponding temperatures (298.15 K, 303.15 K and 308.15 K). The values of ΔH and ΔS can be evaluated from the linear relationship between ln K_{app} and the reciprocal thermodynamic temperature (1/T), and that of ΔG is calculated by Eq. (9).

The calculated values of ΔG, ΔH and ΔS are shown in Table 1. Examination of the enthalpy change and the entropy change suggests that the formation of the AuNPs–HSA conjugate features a favorable enthalpy change ($\Delta H < 0$) that is offset partially by an unfavorable entropy loss ($\Delta S < 0$), resulting in an overall negative free energy change (ΔG). Based on these data and the previous results, we suppose that the association process between AuNPs and HSA is very likely to be mainly affected by electrostatic interaction and hydrogen-bond formation between the positive amino acid residues of HSA and the negative carboxyl group of surface citrate.

Table 1
Apparent binding constant (K_{app}), binding stoichiometry (n) and thermodynamic quantities of the association of HSA with AuNPs.

Temperature (K)	n	K_{app} ($\times 10^8$ M^{-1})	ΔG (kJ mol^{-1})	ΔH (kJ mol^{-1})	ΔS (J mol^{-1} K^{-1})
298.15	11	8.4	−50.9		
303.15	11	2.4	−48.7	−98.4	−160.8
308.15	11	2.3	−49.4		

3.3. Kinetic study of HSA–AuNPs conjugate by time-dependent UV–vis spectra and MCR-ALS

Defining the protein binding kinetics occurring at the nano-interface is recognized for equal importance in the binding thermodynamics for an understanding of protein–nanomaterial conjugate. UV–vis spectral measurements of HSA–AuNPs conjugate evolution in the presence of 13 different concentrations of HSA are performed at three temperatures (298.15 K, 303.15 K and 308.15 K) and their corresponding time-dependent spectra are displayed in Fig. 2 and Figs. S2 and S3 (see Supplementary material). The 13 sets of time-dependent spectra at each temperature are assessed using error theory in factor analysis, either the individual data matrices or the column-wise augmented data matrices. The results show that in any case, only two major components are enough to account for the data set variance. Obviously, the two major components are still AuNPs and AuNPs–HSA conjugate. The column-wise augmented data matrices at three temperatures are then subjected to MCR-ALS analysis using non-negativity constraints (kinetic profiles and spectra), equality constraints (kinetic profile) and normalization (spectra). The initial estimates given in the analysis are the spectra of AuNPs and AuNPs–HSA conjugate resolved above. The final lack of fit, variance explained and similarity coefficient obtained are all below 0.30%, above 99.99% and above 0.9999, respectively, suggesting the validity of all resolutions. Combined with known information about stoichiometric numbers of all species in the reaction and the initial molar concentration of AuNPs, the kinetic profiles of all species in terms of relative concentrations resolved by MCR-ALS can be converted into the desired kinetic profiles in terms of absolute molar concentration (see Fig. 5 and Figs. S6 and S7 in Supplementary material). As can be noticed from the three figures, during the binding process of HSA to the AuNPs surface, the concentrations of AuNPs and HSA decrease exponentially while those of AuNPs–HSA conjugate increase exponentially. In addition, it is clearly seen that the higher the concentrations of HSA, the faster the binding reaction. According to the reaction mechanism proposed above, the reaction rate, v, in terms of rate of change in AuNPs concentration may be expressed as follows [54]:

$$v = -\frac{dc_{HSA}}{dt} = k_a c_{HSA}^{\alpha} \tag{10}$$

where c_{HSA}, k_a and superscript α denote the time-dependent concentration of HSA, the reaction rate constant describing the rate of AuNPs–HSA conjugate formation between AuNPs and HSA, and the order of the reaction with respect to HSA. Taking the natural logarithm of both sides of this equation, it can be expressed as follows:

$$\ln v = \ln k_a + \alpha \ln c_{HSA} \tag{11}$$

To determine the reaction rate constant and the order of the reaction with respect to HSA, the concentration of HSA is simply changed while holding the concentration of AuNPs constant (see Fig. 5 and

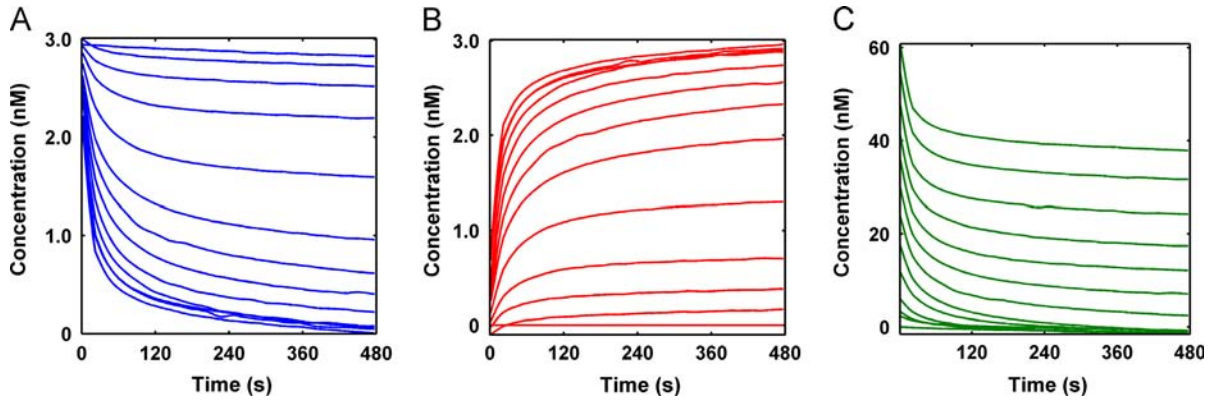

Fig. 5. (A) Kinetic profiles of AuNPs in terms of molar concentration obtained by MCR-ALS on the column-wise augmented matrix from 13 molar-ratio experiments at 298.15 K. (B) Resolved kinetic profiles of AuNPs–HSA conjugate. (C) Resolved kinetic profiles of HSA.

Figs. S6 and S7 in Supplementary material). Then, the initial rate at time 0 can be calculated from the kinetic profiles of HSA. The values of k_a and α can be estimated from the linear relationship between $\ln v$ and $\ln c_{HSA}$. The value of α at three temperatures is calculated to be 0.9, close to 1, suggesting that the reaction likely follows the first-order kinetics. Based on the first-order kinetics, the reaction rate constants (k_a) at 298.15 K, 303.15 K and 308.15 K are calculated as $2.2\times10^{-4}\,s^{-1}$, $2.4\times10^{-4}\,s^{-1}$ and $5.4\times10^{-4}\,s^{-1}$, respectively. It is found that the rate constants increase monotonically as the temperature is raised. The temperature dependence of the rate constants can be evaluated according to the Eyring theory of activation [54]. According to the theory, the activation energy for the binding reaction can be estimated to be $66.6\,kJ\,mol^{-1}$ from the linear relationship between $\ln k_a$ and the reciprocal thermodynamic temperature ($1/T$) [54].

3.4. Spectroscopic biosensor for detection of HSA

In addition to gaining a deep insight into the evolution process of the AuNPs–HSA conjugate, a sensitive spectroscopic biosensor for detection of HSA is further constructed. Fig. 4 clearly indicates the concentration changes of AuNPs and AuNPs–HSA conjugate after the addition of HSA (1.8–70.3 nM). It is found that the concentrations of AuNPs and AuNPs–HSA conjugate are linearly related to the concentration of HSA added (1.8–28.1 nM), with equations of $c_{AuNPs}\,(nM) = -0.082c_{HSA}\,(nM) + 2.81$ ($r=0.996$) and $c_{AuNPs\text{-}HSA}\,(nM) = 0.082c_{HSA}\,(nM) + 0.14$ ($r=0.996$). Limits of detection with a signal-to-noise ratio (S/N) of 3 for both AuNPs and AuNPs–HSA conjugate calibrations are 0.8 nM, which were well comparable or superior to those achieved by sensitive fluorometric methods [55,56].

4. Conclusion

This work describes the first demonstration of UV–vis spectroscopy and multivariate curve resolution by alternating least squares (MCR-ALS) as a combined tool to investigate the evolution of protein nanoconjugate in situ. Human serum albumin (HSA) and citrate-capped gold nanoparticles (AuNPs) are selected as a model of protein and nanomaterial, respectively. It is found that conventional UV–vis spectroscopy provides a preliminary qualitative analysis of the HSA corona binding to AuNPs by observation of spectral changes and leads to the conclusion that AuNPs are coated by HSA to form a stable AuNPs–HSA corona complex. This obtained information is very limited and not enough for relatively comprehensive understanding of the complex. However, the introduction of an MCR-ALS tool strikingly enhances the resolving power of traditional UV–vis spectroscopy, allowing quantitative extraction of the distribution diagrams, spectra and kinetic profiles of absorbing pure species (AuNPs and the AuNPs–HSA corona complex) from the UV–vis spectral data of the complex evolving system. The profiles of all these pure species are conveniently converted into the thermodynamic, kinetic and structural parameters describing the characteristics of the AuNPs–HSA conjugate evolutions. In addition, the concentration evolutions of pure species resolved by MCR-ALS are studied to fabricate the spectroscopic biosensor for HSA. The results show the high sensitivity for HSA, mainly owing to the high molar extinction coefficient of AuNPs and the powerful resolution of MCR-ALS. Although the biosensor lacks selectivity for HSA, it is believed that the selectivity can be partially or greatly enhanced by the second-order advantage of the MCR-ALS algorithm [57–59]. Future work will be conducted to validate the second-order advantage of the proposed method.

Acknowledgments

This work was supported by the National Natural Science Foundation of China (NSFC-21065007 and NSFC-21305061), the Natural Science Foundation of Jiangxi Province (20132BAB213011), the Jiangxi Provincial Department of Education (GJJ13026) and the State Key Laboratory of Food Science and Technology of Nanchang University (SKLF-ZZA-201302 and SKLF-ZZB-201303)

Appendix A. Supplementary material

Supplementary data associated with this article can be found in the online version at http://dx.doi.org/10.1016/j.talanta.2013.11.026.

References

[1] A.E. Nel, L. Madler, D. Velegol, T. Xia, E.M.V. Hoek, P. Somasundaran, F. Klaessig, V. Castranova, M. Thompson, Nat. Mater. 8 (2009) 543–557.
[2] R. Mout, V.M. Rotello, Isr. J. Chem. 53 (2013) 1–9.
[3] S. Rana, Y.C. Yeh, V.M. Rotello, Curr. Opin. Chem. Biol. 14 (2010) 828–834.
[4] P. Wu, L.N. Miao, H.F. Wang, X.G. Shao, X.P. Yan, Angew. Chem. Int. Ed. 50 (2011) 8118–8121.
[5] R.T. Hill, J.B. Shear, Anal. Chem. 78 (2006) 7022–7026.
[6] X.Y. Ouyang, R.Q. Yu, J.Y. Jin, J.S. Li, R.H. Yang, W.H. Tan, J.L. Yuan, Anal. Chem. 83 (2011) 782–789.
[7] J. Bao, W. Chen, T.T. Liu, Y.L. Zhu, P.Y. Jin, L.Y. Wang, J.F. Liu, Y.G. Wei, Y.D. Li, ACS Nano 1 (2007) 293–298.
[8] U.H.F. Bunz, V.M. Rotello, Angew. Chem. Int. Ed. 49 (2010) 3268–3279.
[9] O.R. Miranda, B. Creran, V.M. Rotello, Curr. Opin. Chem. Biol. 14 (2010) 728–736.
[10] S. Mao, G.H. Lu, K.H. Yu, Z. Bo, J.H. Chen, Adv. Mater. 22 (2010) 3521–3526.
[11] P. Pengo, L. Baltzer, L. Pasquato, P. Scrimin, Angew. Chem. Int. Ed. 46 (2007) 400–404.

[12] Y. Jeong, B. Duncan, M.H. Park, C. Kim, V.M. Rotello, Chem. Commun. 47 (2011) 12077–12079.
[13] M.J. Ruedas-Rama, E.A.H. Hall, Anal. Chem. 83 (2010) 9043–9049.
[14] W.J. Goh, V.S. Makam, J. Hu, L.F. Kang, M.R. Zheng, S.L. Yoong, C.N.B. Udalagama, G. Pastorin, Langmuir 28 (2012) 16864–16873.
[15] J.T. Holland, C. Lau, S. Brozik, P. Atanassov, S. Banta, J. Am. Chem. Soc. 133 (2011) 19262–19265.
[16] C. Niemeyer, Angew. Chem. Int. Ed. 42 (2003) 5796–5800.
[17] Y. Xiao, F. Patolsky, E. Katz, J.F. Hainfeld, I. Willner, Science 299 (2004) 1877–1881.
[18] C.C. You, M. De, V.M. Rotello, Curr. Opin. Chem. Biol. 9 (2005) 639–646.
[19] M. Rahman, S. Laurent, N. Tawil, L. Yahia, M. Mahmoudi, Protein-Nanoparticle Interactions: The Bio–Nano InterfaceSpringer Verlag, New York, 2013.
[20] M. Mahmoudi, I. Lynch, M.R. Ejtehadi, M.P. Monpoli, F.B. Bombelli, S. Laurent, Chem. Rev. 111 (2011) 5610–5637.
[21] K.E. Sapsford, K.M. Tyner, B.J. Dair, J.R. Deschamps, I.L. Medintz, Anal. Chem. 83 (2011) 4453–4488.
[22] C.D. Walkey, W.C.W. Chan, Chem. Soc. Rev. 41 (2012) 2780–2799.
[23] T. Cedervall, I. Lynch, S. Lindman, T. Berggard, E. Thulin, H. Nilsson, K.A. Dawson, S. Linse, Proc. Natl. Acad. Sci. USA 104 (2007) 2050–2055.
[24] M. Mahmoudi, M.A. Shokrgozar, S. Sardari, M.K. Moghadam, H. Vali, S. Laurent, P. Stroeve, Nanoscale 3 (2011) 1127–1138.
[25] L.W. Li, Q.X. Zhang, B. Zhang, B. Yan, Analyst 135 (2010) 1519–1530.
[26] B.K. Lavine, J. Workman, Anal. Chem. 85 (2013) 705–714.
[27] V.A. Shashilov, I.K. Lednev, Chem. Rev. 110 (2010) 5692–5713.
[28] J.G. Davis, K.P. Gierszal, P. Wang, D. Ben-Amotz, Nature 491 (2012) 582–585.
[29] J. Jaumot, R. Gargallo, A. De Juan, R. Tauler, Chemometrics Intell. Lab. Syst. 76 (2005) 101–110.
[30] J. Jaumot, R. Gargallo, A. De Juan, R. Tauler, J. Am. Chem. Soc. 131 (2009) 4378–4386.
[31] S. Navea, R. Tauler, A. De Juan, Anal. Chem. 78 (2006) 4768–4778.
[32] K. Wongravee, T. Parnklang, P. Pienpinijtham, C. Lertvachirapaiboon, Y. Ozaki, C. Thammacharoen, S. Ekgasit, Phys. Chem. Chem. Phys. 15 (2013) 4183–4189.
[33] J.M.M. Leitao, H. Goncalves, C. Mendonca, J.C.G.E. Da Silva, Anal. Chim. Acta 628 (2008) 143–154.
[34] M. Rivallan, E. Seguin, S. Thomas, M. Lepage, N. Takagi, H. Hirata, F. Thibault-Starzyk, Angew. Chem. Int. Ed. 49 (2010) 785–789.
[35] E.R. Malinowski, M. Barber, J.G.T. Whitaker, E.T. Smith, J. Chemometrics 21 (2007) 520–528.
[36] X.M. He, D.C. Carter, Nature 358 (1992) 209–215.
[37] M.L. Ferrer, R. Duchowicz, B. Carrasco, J.G. De La Torre, A.U. Acuna, Biophys. J. 80 (2001) 2422–2430.
[38] K. Saha, S.S. Agasti, C. Kim, X.N. Li, V.M. Rotello, Chem. Rev. 112 (2012) 2739–2779.
[39] T. Peters, All About Albumins: Biochemistry, Genetics and Medical ApplicationsAcademic Press, San Diego, 1996.
[40] K.C. Grabar, R.G. Freeman, M.B. Hommer, M.J. Natan, Anal. Chem. 67 (1995) 735–743.
[41] X.H. Ji, X.N. Song, J. Li, Y.B. Bai, W.S. Yang, X.G. Peng, J. Am. Chem. Soc. 129 (2007) 13939–13948.
[42] W. Haiss, N.T.K. Thanh, J. Aveyard, D.G. Fernig, Anal. Chem. 79 (2007) 4215–4221.
[43] S.H. Brewer, W.R. Glomm, M.C. Johnson, M.K. Knag, S. Franzen, Langmuir 21 (2005) 9303–9307.
[44] Y.N. Hong, C. Feng, Y. Yu, J.Z. Liu, J.W.Y. Lam, K.Q. Luo, B.Z. Tang, Anal. Chem. 82 (2010) 7035–7043.
[45] T.J. Lenk, B.D. Ratner, R.M. Gendreau, K.K. Chittur, J. Biomed. Mater. Res. 23 (1989) 549–569.
[46] P. Wulandari, X.H. Li, K. Tamada, M. Hara, J. Nonlinear Opt. Phys. Mater. 17 (2008) 185–192.
[47] T.J. Lenk, T.A. Horbett, B. Ratner, K.K. Chittur, Langmuir 7 (1991) 1755–1764.
[48] M. Vives, R. Gargallo, R. Tauler, Anal. Chem. 71 (1999) 4328–4337.
[49] N. Li, S. Zeng, L. He, W.W. Zhong, Anal. Chem. 82 (2010) 7460–7466.
[50] C. Rocker, M. Potzl, F. Zhang, W.J. ParakG.U.A. Nienhaus, Nat. Nanotechnol. 4 (2009) 577–580.
[51] W. Jiang, B.Y.S. Kim, J.T. Rutka, W.C.W. Chan, Nat. Nanotechnol. 3 (2008) 145–150.
[52] T.M. Lovestead, T.J. Bruno, Anal. Chem. 82 (2010) 5621–5627.
[53] P. Atkins, J. De Paula, Physical ChemistryW.H. Freeman and Company, New York, 2006.
[54] R.G.N. Wilkins, Kinetics and Mechanisms of Reactions of Transition Metal ComplexesVCH Publishers, Weinheim, 1991.
[55] Y.N. Hong, C. Feng, Y. Yu, J.Z. Liu, J.W.Y. Lam, K.Q. Luo, B.Z. Tang, Anal. Chem. 82 (2010) 7035–7043.
[56] X.J. Xu, J. Huang, J.J. Li, J.W. Yan, J.G. Qin, Z. Li, Chem. Commun. 47 (2011) 12385–12387.
[57] S.A. Bortolato, J.A. Arancibia, G.M. Escandar, Anal. Chem. 81 (2009) 8074–8084.
[58] P. Pasamontes, M.P. Callao, Trends Anal. Chem. 25 (2006) 77–85.
[59] M. Vosough, H.M. Esfahani, Talanta 113 (2013) 68–75.